



# The growth of self-intercalated $\text{Nb}_{1+x}\text{Se}_2$ by molecular beam epitaxy: The effect of processing conditions on the structure and electrical resistivity

Peter M. Litwin<sup>1</sup>, Samantha T. Jaszewski<sup>1</sup>, Wendy L. Sarney<sup>2</sup>, Asher C. Leff<sup>2,3</sup>, Sergiy Krylyuk<sup>4</sup>, Albert V. Davydov<sup>4</sup>, Jon F. Ihlefeld<sup>1,5</sup>, Stephen J. McDonnell<sup>1,a)</sup>

<sup>1</sup>Department of Materials Science and Engineering, University of Virginia, Charlottesville, VA, USA

<sup>2</sup>CCDC Army Research Laboratory, Adelphi, MD, USA

<sup>3</sup>General Technical Services, LLC, Wall, NJ, USA

<sup>4</sup>Materials Science and Engineering Division, National Institute of Standards and Technology, Gaithersburg, MD, USA

<sup>5</sup>Department of Electrical and Computer Engineering, University of Virginia, Charlottesville, VA, USA

a) Electronic mail: sjm3qf@virginia.edu

We report on the synthesis of self-intercalated (SI)  $\text{Nb}_{1+x}\text{Se}_2$  thin films by molecular beam epitaxy (MBE).  $\text{Nb}_{1+x}\text{Se}_2$  is a metal-rich phase of  $\text{NbSe}_2$  where additional Nb atoms populate the van der Waals gap. The grown thin films are studied as a function of the Se to Nb beam equivalence pressure ratio (BEPR). X-ray photoelectron spectroscopy (XPS) and x-ray diffraction (XRD) indicate that BEPRs of 5:1 and greater result in the growth of the  $\text{Nb}_{1+x}\text{Se}_2$  phase and that the amount of intercalation is inversely proportional to the Se to Nb BEPR. Electrical resistivity measurements also show an inverse relationship between BEPR and resistivity in the grown  $\text{Nb}_{1+x}\text{Se}_2$  thin films. A second Nb-Se compound with a stoichiometry of ~1:1 was synthesized using a Se to Nb BEPR of 2:1; in contrast to the  $\text{Nb}_{1+x}\text{Se}_2$  thin films, this compound did not show evidence of a layered structure.

## I. INTRODUCTION

The self-intercalation (SI) of metal-rich, group-VB transition metal dichalcogenides (TMDCs) has recently gained attention as a method to tune the properties, including ferromagnetic order and catalytic performance, of metallic TMDCs<sup>1-3</sup>. SI refers to the intercalation of surplus transition metal atoms into the van der Waals gap of the TMDC taking the form  $M_{1+x}Ch_2$ , where  $M$ ,  $Ch$ , and  $x$  refer to the transition metal, chalcogen, and occupancy of intercalated transition metal atoms, respectively. While these compounds, such as  $Ta_{1+x}S_2$  and  $Nb_{1+x}Se_2$ , have been studied in the bulk since the 1960's, most of the early work was focused on understanding the solubility limits of the metal intercalant and the polymorphism of the bulk layered phases<sup>4-14</sup>. Recent density functional theory (DFT) by Zhao et al. highlights the emergence of ferromagnetism in SI Nb- and Ta-based TMDCs in contrast to their non-ferromagnetic, stoichiometric counterparts, i.e., in the absence of SI<sup>1</sup>. Furthermore, Yang et al. showed experimental evidence of improved catalytic performance of  $Nb_{1.35}S_2$  over  $NbS_2$  due to increased current densities in the former attributed to a partial elimination of the van der Waals gap in the SI compound<sup>2</sup>; this example highlights the use of SI as a method to tune the anisotropy of the material's electrical conductivity. The majority of studies on thin film group-VB TMDCs focus on investigations into charge density wave (CDW) and superconductivity states. However, most reports on these thin film materials involve monolayers<sup>15-24</sup>, whereas studies on multilayer films are scarce. Despite the low number of reports on SI thin film TMDCs, free energies calculated with DFT by Sidoumou et al.<sup>25</sup> and Zhao et al.<sup>1</sup> on the group-VB TMDCs show comparable stability between the SI and non-intercalated structures suggesting that the growth of SI, group-VB TMDC thin films should be common in multilayer films. The growth of  $Nb_{1+x}Se_2$  was speculated in the works of Shimada et al.<sup>13, 26</sup> based on the formation of the 3R and 2H<sub>b</sub> polytypes; these polytypes have been shown to form in the presence of excess Nb in bulk samples<sup>11</sup>. However, no direct evidence of SI in either of the works

by Shimada was reported and to date there lacks conclusive reports of thin film synthesis of SI  $\text{Nb}_{1+x}\text{Se}_2$ .

Here we report on the synthesis of multilayer  $\text{Nb}_{1+x}\text{Se}_2$  thin films grown by molecular beam epitaxy (MBE) on  $\text{SiO}_2$ . We study the effect of altering the Se to Nb beam equivalence pressure ratio (BEPR) used during the growth on the resultant material. At a Se to Nb BEPR of 5:1 and above, the  $\text{Nb}_{1+x}\text{Se}_2$  structure is obtained; in this processing space, increased BEPRs are found to reduce the degree of SI which is detectable by a change in the materials' c-lattice parameter. However, in all cases our multilayer  $\text{NbSe}_2$  films are of the SI, Nb-rich variety, even under BEPRs as high as 45,000:1. We further identify an inverse relationship between the BEPR and the in-plane electrical resistivity indicating that Nb SI is detrimental to the electrical conductivity. At a BEPR of 2:1 an additional Nb-Se compound was formed with ~1:1 stoichiometry; this compound showed no evidence of a layered structure.

## II. Methods

$\text{NbSe}_x$  thin films were grown by MBE on 285 nm thick  $\text{SiO}_2$ /highly p-doped Si(100) substrates (Graphene Supermarket). The substrates were rinsed in acetone followed by isopropanol, and blown dry with  $\text{N}_2$  gas. The samples were clamped to a Mo sample holder using strips of Ta foil which were spot welded to the holder. All samples were exposed to a 5-minute UV- $\text{O}_3$  treatment just before being introduced into vacuum to remove any adsorbed contaminants. Once in ultra-high vacuum (base pressure  $\sim 1 \times 10^{-9}$  mBar), the substrates were first held at 245 °C for 12 h. Then, prior to growth, the substrate was heated to 800 °C and held there for 10 minutes to remove any physisorbed species from the substrate. The substrate was then cooled down to the growth temperature of 770 °C. Se (99.999% pellets, Kurt J. Lesker) was evaporated from a standard effusion cell and Nb (99.9%, rod, Goodfellow Cambridge Ltd.) was evaporated from a

Focus EFM-4 UHV e-beam evaporator. The Nb rod was evaporated using a constant heating power (constant emission current and voltage). The heating power of Nb was set to provide a beam equivalence pressure (BEP) of  $2 \times 10^{-9}$  mBar as determined by a beam flux monitor placed in the path of the Nb beam prior to growth; this beam pressure was used for the growth of all thin films discussed in this study. The beam pressure of Se was measured in the same way and controlled by altering the source temperature. The range of BEPRs used in this study was accomplished by altering the Se BEP while maintaining a constant Nb BEP. The growth of the thin films discussed in this work was carried out by co-depositing the Nb and Se elemental sources continuously for 5 hours. At the end of the growth, the Nb source was closed, and the films were held at the growth temperature for 2 minutes in a Se flux before turning off the sample heater and allowing the sample to cool in a Se flux for 10 minutes; at this time, the substrate temperature is  $\sim 300$  °C estimated using temperature vs time data collected during sample cool down. This temperature is estimated as it falls below the lower limit of the pyrometer used to monitor substrate temperature. The Se shutter was then closed to avoid Se condensation on the grown thin films. A bulk NbSe<sub>2</sub> crystal, which was used as a reference sample, was synthesized by chemical vapor transport (CVT); details of the CVT growth have been previously published <sup>27</sup>.

In-vacuo x-ray photoelectron spectroscopy (XPS) was carried out using a monochromated Al-K $\alpha$  source (1486.7 eV) at 50 eV pass energy to study the chemical nature of the films. In-situ reflection high-energy electron diffraction (RHEED) was used to characterize the structure of the deposited thin films. In-situ angle resolved photoelectron spectroscopy (ARPES) was carried out using photon energy of 21.22 eV and a pass energy of 2 eV; the photon source is a Focus HIS14 HD VUV source. Further details of the MBE tool and in-situ characterization techniques used are found elsewhere <sup>28</sup>. Ex-situ x-ray diffraction (XRD) was carried out using two diffractometers, a

SmartLab diffractometer from Rigaku and an Empyrean diffractometer from Malvern-Panalytical. XRD measurements were collected in a symmetrical, out-of-plane geometry using Cu K $\alpha$  radiation. All samples underwent a surface normal alignment prior to XRD measurements. High-resolution transmission electron microscopy (HRTEM) and scanning transmission electron microscopy (STEM) was carried out on a probe-corrected JEOL ARM 200F at the Army Research Lab in Adelphi, MD, USA. Average background subtraction filtering (ABSF) using the method described by Kilaas was utilized to remove noise introduced by surface amorphization from HR-TEM and HR-STEM images<sup>29</sup>. Specimens were prepared for TEM via focused ion beam cross-section lift-out using a Thermo Fisher Scientific Helios G4 UX. Sheet resistance measurements were collected using a multiheight probe by Jandel Engineering Limited which utilizes a 4-point probe set up in a linear array; the tips are 40  $\mu\text{m}$  thick and equally spaced 1.00 mm apart. The in-plane electrical resistivity was calculated using the measured sheet resistance, the thickness of the thin films, which was determined using x-ray reflectivity (XRR) measurements, and known correction factors to account for the effects of sample dimensions<sup>30</sup>. XRR measurements were performed on a Panalytical Empyrean with Cu K $\alpha$  radiation. XRR patterns were fit using GSAS-II software<sup>31</sup>.

Data in this study was collected on two sets of samples. One set was used for XPS and XRD measurements and an additional sample set was used for XRR and electrical conductivity measurements. The sample sets were grown in an identical manner.

### III. RESULTS AND DISCUSSION

#### A. *Identification of the Nb<sub>1+x</sub>Se<sub>2</sub> phase*

The XPS spectrum of a ~10 nm MBE-grown NbSe<sub>2</sub> thin film is presented in *Figure 1*. Overlaid with this spectrum is the XPS spectrum of bulk 2H-NbSe<sub>2</sub> grown by CVT which is used

as a reference. Comparing the two spectra, there are additional features in the core-level spectra of the MBE-grown material; this is more pronounced in the Se 3d spectra. Stoichiometry estimates for the MBE-grown material indicate that the sample is Nb-rich approximating  $\text{Nb}_{1.18}\text{Se}_2$  for the sample represented in *Figure 1*. The stoichiometry was estimated using the total Nb and Se 3d intensities and comparing them to those seen in the CVT-grown 2H-NbSe<sub>2</sub> reference sample which is assumed to be a 2:1 stoichiometry.

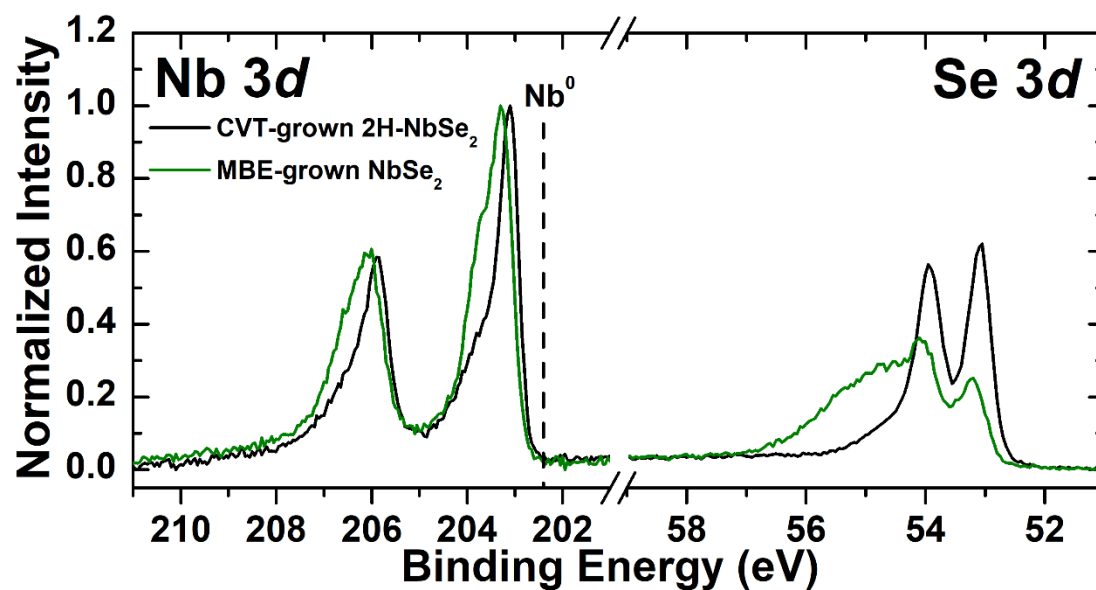


Figure 1: XPS spectra of CVT 2H-NbSe<sub>2</sub> (black) and MBE-grown NbSe<sub>2</sub> (green). The MBE-NbSe<sub>2</sub> thin film was grown with a Se to Nb BEPR of 1600:1.

The XRD pattern of ~10 nm MBE-grown NbSe<sub>2</sub> can be seen in *Figure 2* (along with data of the CVT-grown 2H-NbSe<sub>2</sub> crystal). In both samples only the out-of-plane (*00l*) reflections are present, indicative of a layered structure. The broader peaks present in the MBE-grown NbSe<sub>2</sub> sample are attributed to Scherrer broadening due to the ~10 nm sample thickness. The clear shift

of the 002 peak (along with higher order reflections) to lower  $2\theta$  angles in the MBE-grown material is indicative of an expanded lattice constant along the c-axis, perpendicular to the NbSe<sub>2</sub> basal plane. The out-of-plane lattice constant was quantified through analysis of the 00 $l$  planes ( $l = 2, 4, 6,$  and  $8$ ) using the Nelson-Riley extrapolation method<sup>32</sup>. For the CVT-grown 2H sample, the out-of-plane lattice constant was found to be 12.54 Å, consistent with previous reports of stoichiometric 2H-NbSe<sub>2</sub> of 12.54-12.55 Å<sup>7, 8, 14</sup>. For the MBE-grown NbSe<sub>2</sub> film represented in *Figure 2*, the out-of-plane lattice constant was found to be 13.06 Å, a ~4% increase over the CVT-grown 2H-NbSe<sub>2</sub> sample. XRD features labeled *Substrate/stage* were assigned by performing XRD on a bare SiO<sub>2</sub>/Si sample which contained these features and are therefore not related to the NbSe<sub>2</sub> film studied here (*see supplementary material at [URL will be inserted by AIP Publishing]*).

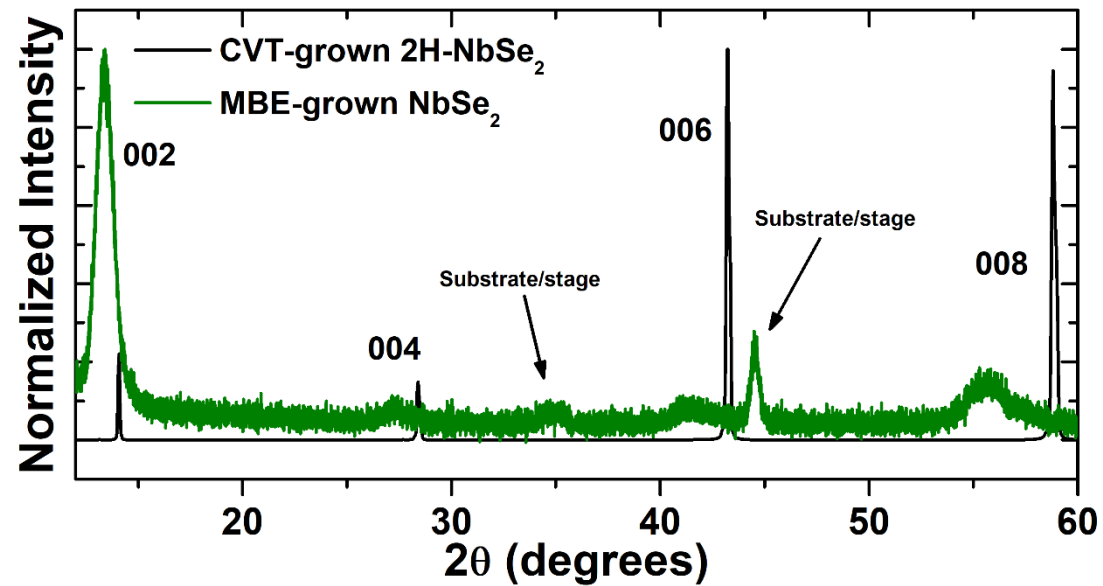


Figure 2: XRD of CVT-grown 2H-NbSe<sub>2</sub> (black) and ~10 nm MBE-grown NbSe<sub>2</sub> on SiO<sub>2</sub> (green). The MBE-NbSe<sub>2</sub> thin film was grown with a Se to Nb BEPR of 1600:1.

*Figure 3a* shows an HRTEM cross-section view of the NbSe<sub>2</sub> sample perpendicular to the c-axis with the zone axes corresponding to [120] NbSe<sub>2</sub>/Si [ $\bar{1}10$ ]. This NbSe<sub>2</sub> film was grown with a BEPR of 1600:1. Also in the image are the SiO<sub>2</sub> substrate and expected NbO<sub>x</sub>, as well as IrO<sub>x</sub> and Pt layers deposited during sample preparation. The image shows that the film is layered; i.e., the basal plane of all the NbSe<sub>2</sub> layers are aligned, which agrees with the XRD results. Additionally, the film is uniform, and no additional phases or structures are apparent. *Figure 3b* shows a higher magnification, ABSF HRTEM image of the same sample. The periodicity along the c-axis is 4 atoms which differs from the expected periodicity along the c-axis of NbSe<sub>2</sub> which is 3 atomic layers. The ABSF filtered, high angle annular dark field STEM image (zone axes [100] NbSe<sub>2</sub>/Si [110]) in *Figure 3c* further highlights the layered structure of NbSe<sub>2</sub> (bright field STEM image included in *supplementary material at [URL will be inserted by AIP Publishing]*). Also apparent in the image is a periodic signal residing in the van der Waals gap between the adjacent NbSe<sub>2</sub> layers consistent with the HRTEM image in *Figure 3b* (marked SI-Nb). STEM imaging was collected on a NbSe<sub>2</sub> thin film grown with a Se to Nb BEPR of 5:1.

This is the author's peer reviewed, accepted manuscript. However, the online version of record will be different from this version once it has been copyedited and typeset.  
PLEASE CITE THIS ARTICLE AS DOI: 10.1116/6.0002593

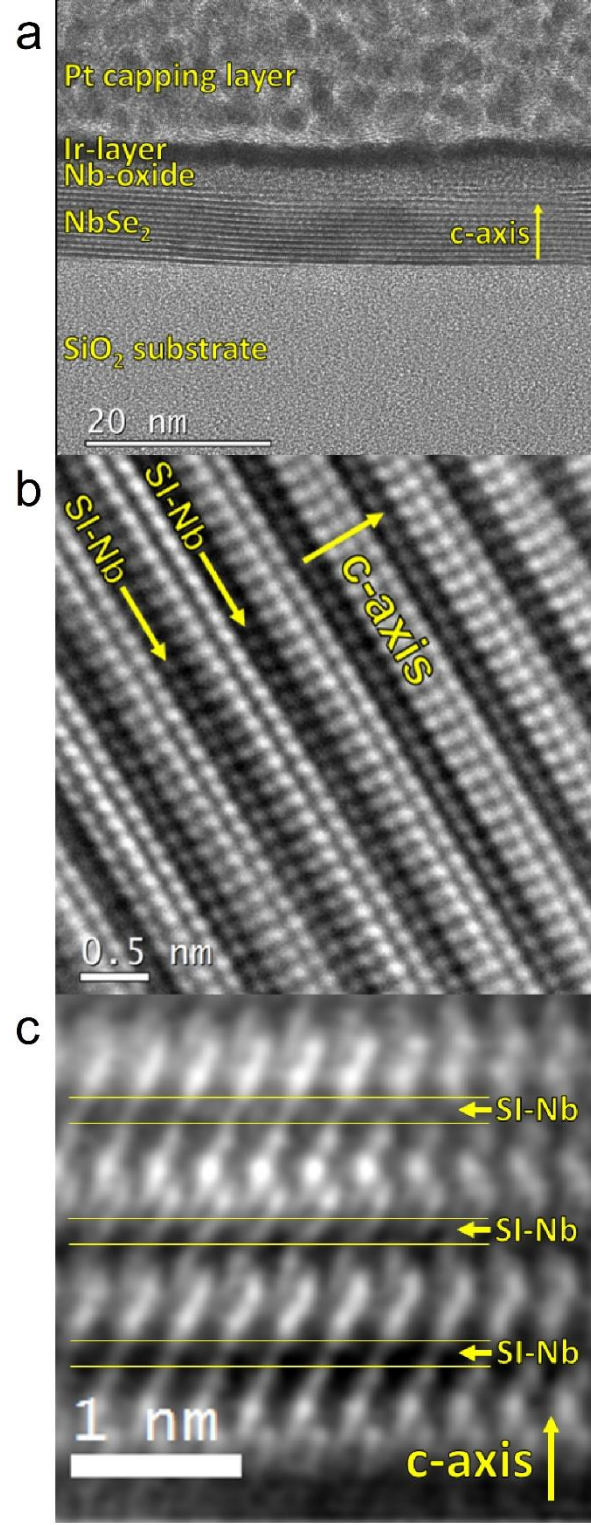


Figure 3: HRTEM (*frames a and b*) and high angle annular dark field STEM (*frame c*) images of ~10 nm MBE-grown NbSe<sub>2</sub>. Yellow lines in *c* highlight additional atoms in the van der Waals gap, marked SI-Nb. HRTEM and STEM images were taken on the MBE-NbSe<sub>2</sub> thin films grown at Se to Nb BEPR of 1600:1 and 5:1, respectively.

The deviations in the XPS and XRD of multilayer MBE-grown NbSe<sub>2</sub> with respect to the CVT-grown 2H-NbSe<sub>2</sub> sample indicate the MBE-grown NbSe<sub>2</sub> is Nb-rich and has an expanded *c*-lattice constant. HRTEM/STEM identify a change in periodicity along the *c*-axis compared to the expected structure of stoichiometric NbSe<sub>2</sub>. These three observations are all consistent with the growth of self-intercalated (SI) Nb<sub>1+x</sub>Se<sub>2</sub>. Furthermore, the estimated stoichiometry of Nb<sub>1.18</sub>Se<sub>2</sub> falls in the previously observed composition range for the bulk Nb<sub>1+x</sub>Se<sub>2</sub> compound which was determined to be  $0 < x < 0.29$ <sup>7</sup>. In the Nb<sub>1+x</sub>Se<sub>2</sub> phase, excess Nb atoms populate the van der Waals gap which separates adjacent NbSe<sub>2</sub> slabs as depicted by the ball and stick model in *Figure 4* (here the SI Nb atoms (orange atoms) are partially filled in to represent partial occupancy). Specifically, SI Nb atoms have been observed to reside in the octahedral sites between adjacent NbSe<sub>2</sub> layers in the bulk Nb<sub>1+x</sub>Se<sub>2</sub> compound<sup>11, 14</sup>. This location of the SI Nb is consistent with the STEM image of the MBE-grown material in *Figures 3c*. Additionally, the low contrast associated with the signal in the van der Waals gap observed with STEM imaging is consistent with the expected partial occupancy of these sites.

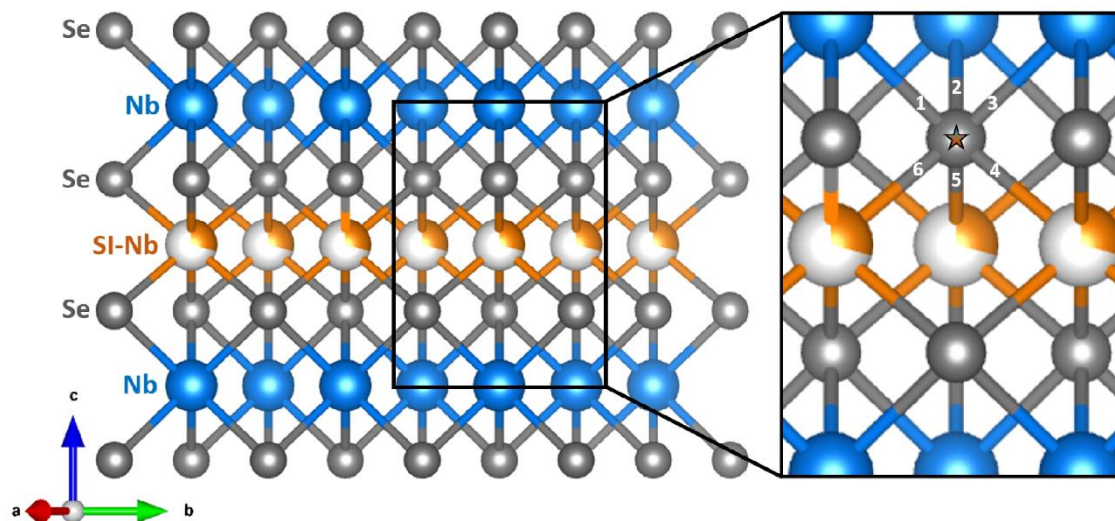


Figure 4: Ball and stick structural model of  $\text{Nb}_{1+x}\text{Se}_2$  phase viewed along the  $[210]$  axis. Se atoms are grey in color. Nb atoms originating from the  $\text{NbSe}_2$  slab are blue. SI Nb atoms are white with a partially shaded in orange area to represent partial occupancy. Right-side of the image highlights how the coordination of a given Se atom (marked with star) changes in the presence of 1, 2 or 3 SI-Nb atoms. Grey/blue lines represent bonds between Se and Nb of a given layer. Grey/orange lines represent bonds between Se and SI-Nb atoms. Ball and stick model created in VESTA<sup>33</sup> with structural model taken from Sidoumou et al.<sup>25</sup>.

The deviations in the XPS spectrum of the MBE-grown  $\text{NbSe}_2$  sample from the CVT-grown 2H- $\text{NbSe}_2$  sample can be explained by considering the consequence of SI Nb atoms located in octahedral sites between adjacent  $\text{NbSe}_2$  slabs in the MBE-grown film. The deviations seen in the Se  $3d$  core level are a result of changes in the atomic coordination of Se atoms in proximity to the intercalated Nb atoms; the altered atomic coordination of these Se atoms alters their oxidation state resulting in unique chemical shifts compared to stoichiometric  $\text{NbSe}_2$ . XPS shows a superposition of all present Se oxidation states which explains the broad Se  $3d$  core level. The

change in coordination of Se atoms can be understood by focusing on a single Se atom and observing how the coordination changes with the addition of SI Nb atoms. As shown in *Figure 4*, coordination of the Se atom (marked with star) is 3 (grey/blue lines) in the absence of SI Nb atoms, but changes to 4, 5 or 6 (grey/orange lines) in the presence of 1, 2 or 3 SI Nb atoms, respectively. The effect of SI on the coordination of metal-rich TMDCs has previously been discussed by Selte and Kjekshus <sup>7</sup>. From the XPS spectra it can be determined that the Se 3*d* core level feature associated with stoichiometric NbSe<sub>2</sub> sits at ~53.1 eV with additional chemical features due to the SI Nb atoms found at higher binding energy. This interpretation of the data is consistent with the work of Bonilla et al. who observed high binding energy components in the Se 3*d* spectra of V-rich VSe<sub>2</sub> which was attributed to SI <sup>34</sup>. In contrast, the coordination of all Nb atoms is 6 (whether the Nb signal originated from the NbSe<sub>2</sub> slab or a SI Nb atom). For this reason, the changes in the Nb 3*d* spectra of the MBE-grown NbSe<sub>2</sub> compared to that of the CVT-grown 2H-NbSe<sub>2</sub> sample are more subtle. The changes in the Nb 3*d* spectra are most likely a consequence of 2<sup>nd</sup> nearest neighbor effects. The XPS of SI Nb<sub>1.27</sub>Se<sub>2</sub> has been studied previously by Khyzhun and in contrast to the work here, no significant broadening of the Se and Nb core levels were observed when compared to stoichiometric NbSe<sub>2</sub> <sup>35</sup>. However, this previous work was carried out with a conventional Mg K $\alpha$  x-ray source rather than a monochromated x-ray source which has been employed here. As such, our present work is expected to have markedly higher resolution. Furthermore, the work by Khyzhun looked at bulk Nb<sub>1.27</sub>Se<sub>2</sub> crystals in contrast to the thin film Nb<sub>1+x</sub>Se<sub>2</sub> materials studied here. These reasons could explain some of the discrepancies observed between the two works.

## **B. The Effect of BEPR**

The chemistry of the MBE-grown NbSe<sub>2</sub> thin films was studied as a function of BEPR. The Se to Nb BEPRs were varied from ~0:1 (no intentional Se flux) to 45,000:1. For the deposition of Nb with no intentional Se flux, though the Se source was left unheated, a residual pressure of Se species was present in the chamber. Measuring this pressure with a residual gas analyzer, suggests an effective BEPR of >0.001:1 during growth. The XPS of the grown thin films can be seen in *Figure 5* and reveals three distinct spectra shapes. The four highest BEPRs, i.e., 5:1, 22:1, 1,600:1 and 45,000:1, all produced similar XPS spectra with estimated stoichiometries ranging from Nb<sub>1.15</sub>Se<sub>2</sub> to Nb<sub>1.23</sub>Se<sub>2</sub>. The growth carried out at a BEPR of 2:1 produced a film with a nearly 1:1 stoichiometry with no evidence of chemical inhomogeneity; the RHEED pattern of this compound is diffuse indicating poor crystallinity (*see supplementary material at [URL will be inserted by AIP Publishing]*). Due to lack of crystallinity, the exact nature of this film is unknown, but it is possibly related to either the bulk compounds Nb<sub>3</sub>Se<sub>4</sub> or Nb<sub>5</sub>Se<sub>4</sub>. Lastly, the growth using no intentional Se flux produced a mix of Nb<sup>0</sup> and an additional NbSe<sub>x</sub> compound.

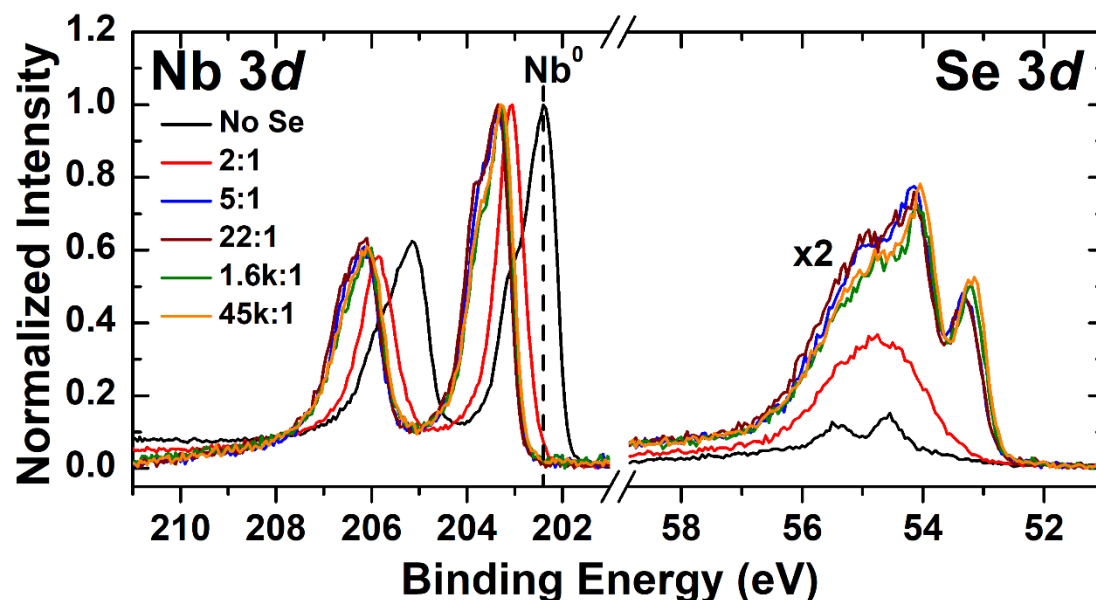


Figure 5: XPS spectra as a function of Se to Nb BEPR used during growth. Se 3d amplitude doubled for clarity.

NbSe<sub>2</sub> thin films grown with Se to Nb BEPRs from 5:1 to 45,000:1 were studied with XRD. *Figure 6a* shows the 002 reflections of the MBE-grown NbSe<sub>2</sub> thin films (the same data plotted on a log-scale is included in the *supplementary material* at [URL will be inserted by AIP Publishing]). Marked on the plot is the position of the expected 002 peak position of bulk, stoichiometric 2H-NbSe<sub>2</sub> which is at higher  $2\theta$  compared to the data collected of the MBE-grown NbSe<sub>2</sub> films in this work. As previously discussed, this difference in peak position is indicative of an expanded c-lattice parameter in the MBE-grown NbSe<sub>2</sub> films compared to the bulk, stoichiometric compound. There is a clear BEPR dependence of the 002 peak, i.e., higher Se to Nb BEPRs result in larger  $2\theta$  for the 002 reflection indicating that the c-lattice parameter is inversely related to the BEPR. The extracted out-of-plane lattice constants collected of the MBE-

grown NbSe<sub>2</sub> in this work valued 13.03, 13.06, and 13.18 Å for thin films grown at 45.000:1, 1,600:1, and 22:1, respectively.

To offer some understanding of how SI Nb impacts the functional properties of the materials, the in-plane electrical resistivity of the MBE-grown NbSe<sub>2</sub> thin films was also studied as a function of Se to Nb BEPR. This is seen to follow an inverse trend in the range of  $2.55 \times 10^{-4}$  to  $7.40 \times 10^{-4}$  Ω-cm (*Figure 6c*). As a reference, previous reported values for stoichiometric bulk NbSe<sub>2</sub> are overlaid onto the plot in *Figure 6c*. The lowest electrical resistivity measured of the MBE-grown samples reported here fall between those previously reported by Brixner<sup>4</sup> and those reported by Maren and Harland<sup>36</sup>. Additional analysis of electrical and thermal transport in our MBE-grown NbSe<sub>2</sub> was recently published by our collaborators<sup>27</sup>.



This is the author's peer reviewed, accepted manuscript. However, the online version of record will be different from this version once it has been copyedited and typeset.  
PLEASE CITE THIS ARTICLE AS DOI: 10.1116/1.6.0002593

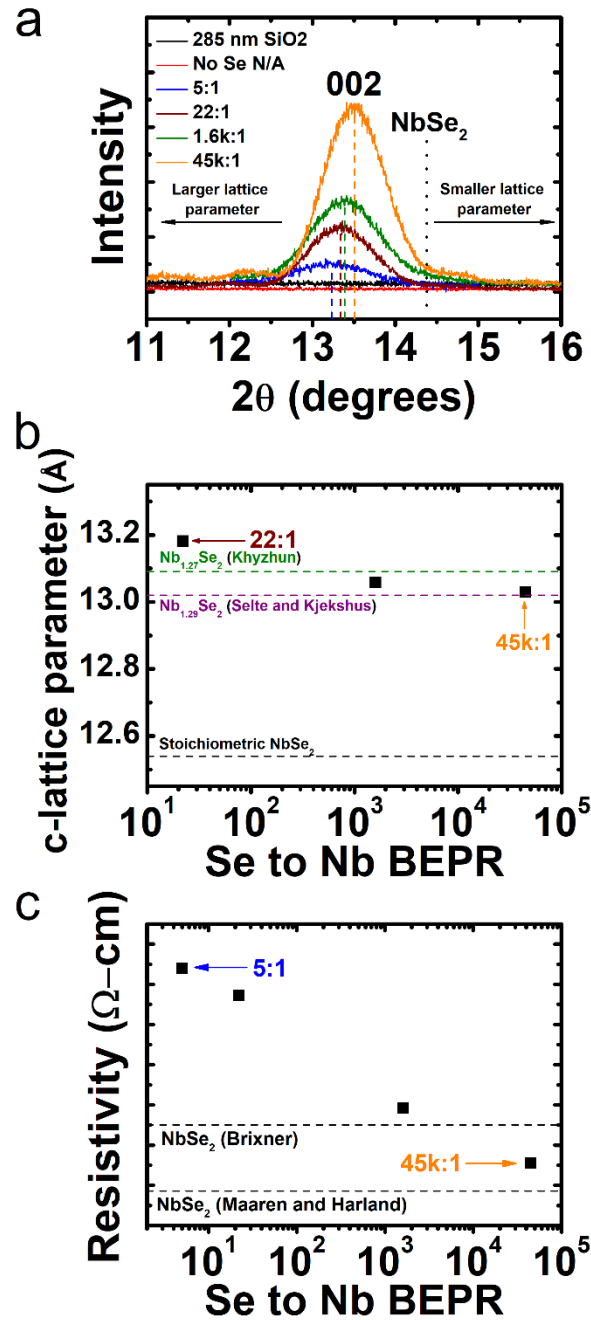


Figure 6: a) XRD scans in the vicinity of the 002 reflections of MBE-grown NbSe<sub>2</sub>, b) extrapolated lattice constants compared to literature values, and c) in-plane electrical resistivity as a function of Se to Nb BEPR used during growth. Lattice constants inset into *b* taken from <sup>7</sup> and <sup>35</sup>. Resistivity values inset onto *c* taken from <sup>4</sup> and <sup>36</sup>.

The observed XPS and XRD results suggest that at BEPRs of 5:1 and greater, the SI  $\text{Nb}_{1+x}\text{Se}_2$  phase is formed. In this processing space, the XPS core-level line-shapes are consistent and the estimated compositions are all within the previously reported composition range of the  $\text{Nb}_{1+x}\text{Se}_2$  structure ( $x = 0$  to  $0.29$ )<sup>7</sup>. We do not observe a direct correlation between varying BEPR and stoichiometry above BEPRs of 5:1 and this is likely due to the error in stoichiometry estimates with XPS which are ~5%; this degree of error was established through the stoichiometric analysis of nominally identical samples. XRD reveals the expected  $00l$  reflections are present in each sample produced under these conditions. Additionally, RHEED patterns observed for the films grown in this processing space suggest there are no significant changes in the in-plane lattice constant or surface morphology. The inverse relationship between Se to Nb BEPR and  $c$ -lattice parameter (*Figure 6b* and *Table I*) follows the trend expected in the presence of SI Nb, i.e., higher Se flux during growth results in a smaller lattice constant; this decrease in lattice constant is due to a decrease in SI Nb under increased Se flux. Selte and Kjekshus measured the out-of-plane lattice constant as a function of stoichiometry and observed a maximum value of  $13.02 \text{ \AA}$  at the solubility limit of the  $\text{Nb}_{1+x}\text{Se}_2$  phase ( $x = 0.29$ )<sup>7</sup>. However, Khyzhun reported a value of  $13.09 \text{ \AA}$  for the bulk  $\text{Nb}_{1.27}\text{Se}_2$  compound, putting some uncertainty in the maximum expected out-of-plane lattice constant<sup>35</sup>. The extracted lattice constants of the MBE-grown  $\text{NbSe}_2$  produced in this work are generally higher than what would be expected. The reason for the increase in out-of-plane lattice constant between the MBE-grown material and previous reports is not fully understood; however, it may relate to the thin film nature of the  $\text{NbSe}_2$  presented here.

The in-plane electrical resistivity follows an inverse relationship to the BEPR, and thus it is concluded that SI Nb increases the in-plane electrical resistivity of  $\text{Nb}_{1+x}\text{Se}_2$  thin films (*Figure 6c* and *Table I*). This increase in resistivity is likely a consequence of an increase in scattering sites

associated with the SI Nb. The resistivity values of all the MBE-grown films are higher than the value reported by Maaren and Harland, which was carried out on stoichiometric single crystals<sup>36</sup>; this result is explained by the absence of both SI Nb and grain boundaries in their single crystals. The resistivity measured by Brixner<sup>4</sup> is higher than that of Maaren and Harland<sup>36</sup> due to polycrystallinity and residual porosity in the pressed and sintered samples.

Table I: Effect of processing conditions on estimated stoichiometry, c-lattice parameter, sample thickness (determined from XRR), and in-plane electrical resistivity. All samples were grown over the course of five hours.

Se to Nb	Estimated	c-lattice	Sample	Electrical Resistivity
BEPR	Stoichiometry	parameter (Å)	Thickness (nm)	(x 10 <sup>-4</sup> Ω-cm)
2:1	Nb <sub>2.14</sub> Se <sub>2</sub>	(non-layered)	-	-
5:1	Nb <sub>1.15</sub> Se <sub>2</sub>	-	10.0	7.40
22:1	Nb <sub>1.20</sub> Se <sub>2</sub>	13.18	9.9	6.72
1,600:1	Nb <sub>1.18</sub> Se <sub>2</sub>	13.06	10.3	3.92
45,000:1	Nb <sub>1.23</sub> Se <sub>2</sub>	13.03	7.2	2.55

Though control over the SI Nb occupancy is demonstrated through alteration of the BEPR used during growth, none of the processing parameters used in this work yielded stoichiometric NbSe<sub>2</sub> in the absence of Nb-intercalation. This is concluded from XPS, which indicates chemical variability remains under the highest BEPRs used (*Figure 5*), and XRD, which indicates the c-lattice parameter of stoichiometric NbSe<sub>2</sub> is never obtained (*Figure 6a* and *6b*). Additionally, the Nb-Se system studied here is comparatively insensitive to changes in BEPR when compared to the

Ta-S system investigated by Zhao et al., who demonstrated complete elimination of SI through an increase of the S to Ta flux ratio <sup>1</sup>. Recent DFT work by Sidoumou et al. suggests that the free energy of Nb<sub>1+x</sub>Se<sub>2</sub> is comparable for  $x=0$  and  $x=0.1$  at the growth temperature used in this work <sup>25</sup>. Since both structures show a similar theoretical stability, it is likely that kinetic factors play a role in the formation of SI Nb<sub>1+x</sub>Se<sub>2</sub>. Zhao et al. performed additional DFT work suggesting the formation energy of Nb<sub>1.17</sub>Se<sub>2</sub> was below that of NbSe<sub>2</sub> at elevated temperatures, again suggesting the formation of SI, multilayer Nb<sub>1+x</sub>Se<sub>2</sub> is preferred <sup>1</sup>. Though beyond the scope of this study, evidence for SI was also observed for MBE-NbSe<sub>2</sub> grown at 370 °C. This suggests SI is not limited to the higher temperature of 770 °C explore in this work.

To date, few works have focused on the growth of multilayer NbSe<sub>2</sub> by MBE making it difficult to compare our work to other MBE-grown NbSe<sub>2</sub>. However, the XPS of our MBE-grown NbSe<sub>2</sub> looks similar to the recent publication of Calavalle et al.; in their work, 1- to 2-layer NbSe<sub>2</sub> was synthesized on graphene/graphite substrates and XPS revealed high binding energy components in the Se 3*d* spectra similar to what is reported in our work here <sup>37</sup>. Calavalle et al. assigned the chemical diversity of Se to the presence of elemental Se formation alongside the intended NbSe<sub>2</sub> layers; high temperature XPS of samples grown in our work rule out the possibility of elemental Se on the surface of our thin films (*Figure S2*). The presence of bilayer regions in the films produced by Calavalle et al. opens the possibility of Nb SI in their grown material. Their study further observed that the intensity of the high binding energy Se component in XPS was greater for NbSe<sub>2</sub> samples which contained more bilayer areas and could therefore be explained by a greater degree of Nb<sub>1+x</sub>Se<sub>2</sub> formation; however, this possibility was not discussed in their publication. A publication by Chen et al. demonstrated strained multilayer NbSe<sub>2</sub> growth by MBE on Al<sub>2</sub>O<sub>3</sub> substrates, which resulted in an expanded c-lattice constant <sup>38</sup>. While we also observe an

expansion in the c-lattice constant of the NbSe<sub>2</sub> multilayer films presented here, the reason for the expansion appears to be of a fundamentally different origin. Substrate-induced strain, as discussed by Chen et al., would not explain the Nb-rich nature of the films deduced from XPS, the structure observed by HRTEM/STEM, nor the BEPR dependencies presented here. Furthermore, the in-plane compression observed by Chen et al. is not consistent with previous reports of the Nb<sub>1+x</sub>Se<sub>2</sub> phase<sup>7</sup>. For these reasons, the c-lattice expansion of the films in our work appears unique from the observations of Chen et al. Additional recent studies have focused on the growth of metastable 1T-NbSe<sub>2</sub><sup>15, 16, 19, 21, 23, 24</sup>. However, 1T-NbSe<sub>2</sub> has been shown to be unstable in bulk samples and thus is unlikely to exist in our multilayer films<sup>39</sup>. Furthermore, synthesis of 1T-NbSe<sub>2</sub> would not explain the Nb-rich nature of the films in this work, the c-lattice expansion observed by XRD, nor the structure observed in HRTEM/STEM.

#### IV. Conclusions

In summary, we demonstrate the synthesis of multilayer Nb<sub>1+x</sub>Se<sub>2</sub> thin films grown on SiO<sub>2</sub> by MBE, which we study as a function of the Se to Nb BEPR. We find that at BEPRs of 5:1 and greater, the SI Nb<sub>1+x</sub>Se<sub>2</sub> phase is grown; this phase is retained up to the maximum BEPR used in this work of 45,000 to 1, albeit with a reduced intercalant occupancy. The electrical resistivity of the Nb<sub>1+x</sub>Se<sub>2</sub> films showed an inverse relationship to the BEPR and a positive correlation with the c-lattice parameter. At BEPRs 2:1 an additional Nb-Se compound with a ~1:1 stoichiometry was synthesized.

#### ACKNOWLEDGMENTS/DISCLAIMER

This work was supported in part by the NSF I/UCRC on Multi-functional Integrated System Technology (MIST) Center; IIP-1439644, IIP-1439680, IIP-1738752, IIP-1939009, IIP-1939050,

and IIP-1939012. Additional support was provided by Intel Corporation. S.T.J. acknowledges support from the U.S. National Science Foundation's Graduate Research Fellowship Program under award DGE-1842490. A.V.D. and S.K. acknowledge support through the Material Genome Initiative funding allocated to the National Institute of Standards and Technology.

NbSe<sub>2</sub> reference single crystals provided by Sergiy Krylyuk.

Disclaimer: Certain commercial equipment, instruments, software or materials are identified in this paper in order to specify the experimental procedure adequately. Such identifications are not intended to imply recommendation or endorsement by the National Institute of Standards and Technology, nor it is intended to imply that the materials or equipment identified are necessarily the best available for the purpose".

## AUTHOR DECLARATIONS

### Conflicts of Interest:

The authors have no conflicts to disclose.

### Author contributions:

**Peter M. Litwin:** Conceptualization (equal); Data curation (lead); Formal analysis (lead); Writing – original draft (lead); Writing – reviewing & editing (equal). **Samantha T. Jaszewski:** Data curation (supporting); Formal analysis (supporting); Writing – review & editing (supporting). **Wendy L. Sarney:** Data curation (supporting); Formal analysis (supporting); Writing – review & editing (supporting). **Asher C. Leff:** Data curation (supporting); Formal analysis (supporting); Writing – review & editing (supporting). **Sergiy Krylyuk:** Data curation (supporting); Writing – review & editing (supporting). **Albert V. Davydov:** Data curation (supporting); Writing – review & editing (supporting). **Jon F. Ihlefeld:** Writing – review &



editing (supporting). **Stephen J. McDonnell**: Conceptualization (equal); Formal analysis (supporting); Funding acquisition (lead); Investigation (lead); Supervision (lead); Writing – review & editing (supporting).

## DATA AVAILABILITY

The data that supports the findings of this study are available within the article and its supplementary material. Additional data that support the findings of this study are available from the corresponding author upon reasonable request.

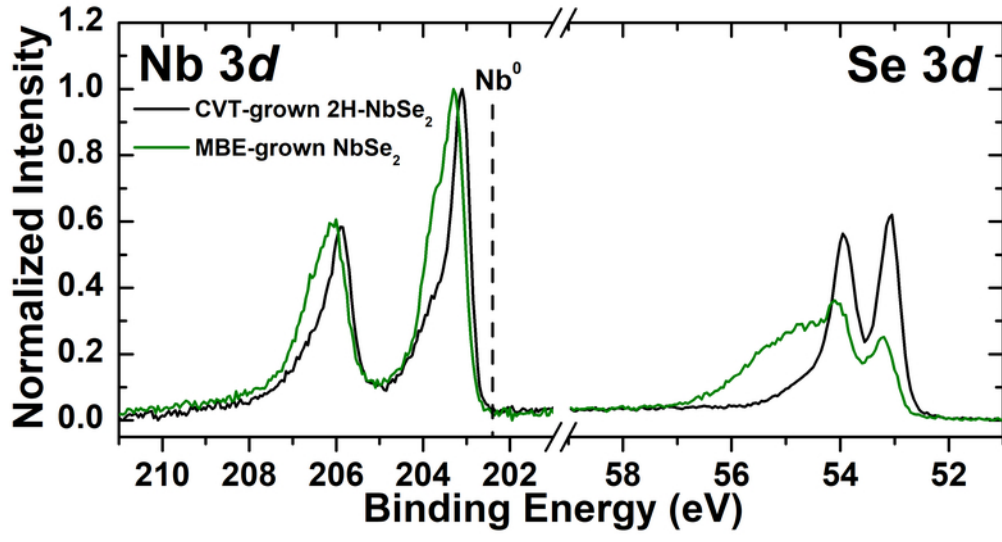
## REFERENCES

1. X. Zhao, P. Song, C. Wang, A. C. Riis-Jensen, W. Fu, Y. Deng, D. Wan, L. Kang, S. Ning, J. Dan, T. Venkatesan, Z. Liu, W. Zhou, K. S. Thygesen, X. Luo, S. J. Pennycook and K. P. Loh, *Nature* **581** (7807), 171-177 (2020).
2. J. Yang, A. R. Mohmad, Y. Wang, R. Fullon, X. Song, F. Zhao, I. Bozkurt, M. Augustin, E. J. G. Santos, H. S. Shin, W. Zhang, D. Voiry, H. Y. Jeong and M. Chhowalla, *Nature Materials* **18** (12), 1309-1314 (2019).
3. A. R. Mohmad, A. A. Hamzah, J. Yang, Y. Wang, I. Bozkurt, H. S. Shin, H. Y. Jeong and M. Chhowalla, *Faraday Discussions* **227** (0), 332-340 (2021).
4. L. H. Brixner, *Journal of Inorganic and Nuclear Chemistry* **24** (3), 257-263 (1962).
5. E. Revolinsky, E. P. Lautenschlager and C. H. Armitage, *Solid State Communications (England-US)* **1** (3), 59-61 (1963).
6. K. Selte and A. Kjekshus, *Acta Crystallographica* **17** (12), 1568-1572 (1964).
7. K. Selte and A. Kjekshus, *Acta chem. scand.* **18**, 697-706 (1964).
8. E. Revolinsky, B. E. Brown, D. J. Beerntsen and C. H. Armitage, *Journal of the Less Common Metals* **8** (1), 63-72 (1965).
9. E. Revolinsky, G. A. Spiering and D. J. Beerntsen, *Journal of Physics and Chemistry of Solids* **26** (6), 1029-1034 (1965).
10. K. Selte and A. Kjekshus, *Acta Chem. Scand* **19** (1) (1965).
11. R. Huisman, F. Kadijk and F. Jellinek, *Journal of the Less Common Metals* **21** (2), 187-193 (1970).
12. K. Igaki and S. Nishine, *Transactions of the Japan Institute of Metals* **20** (5), 219-226 (1979).
13. T. Shimada, Y. Furukawa, E. Arakawa, K. Takeshita, T. Matsushita, H. Yamamoto and A. Koma, *Solid state communications* **89** (7), 583-586 (1994).
14. F. Kadijk, R. Huisman and F. Jellinek, *Recueil des Travaux Chimiques des Pays-Bas* **83** (7), 768-775 (1964).
15. L. Liu, H. Yang, Y. Huang, X. Song, Q. Zhang, Z. Huang, Y. Hou, Y. Chen, Z. Xu, T. Zhang, X. Wu, J. Sun, Y. Huang, F. Zheng, X. Li, Y. Yao, H.-J. Gao and Y. Wang, *Nature Communications* **12** (1), 1978 (2021).
16. Y. Nakata, K. Sugawara, R. Shimizu, Y. Okada, P. Han, T. Hitosugi, K. Ueno, T. Sato and T. Takahashi, *NPG Asia Materials* **8** (11), e321-e321 (2016).

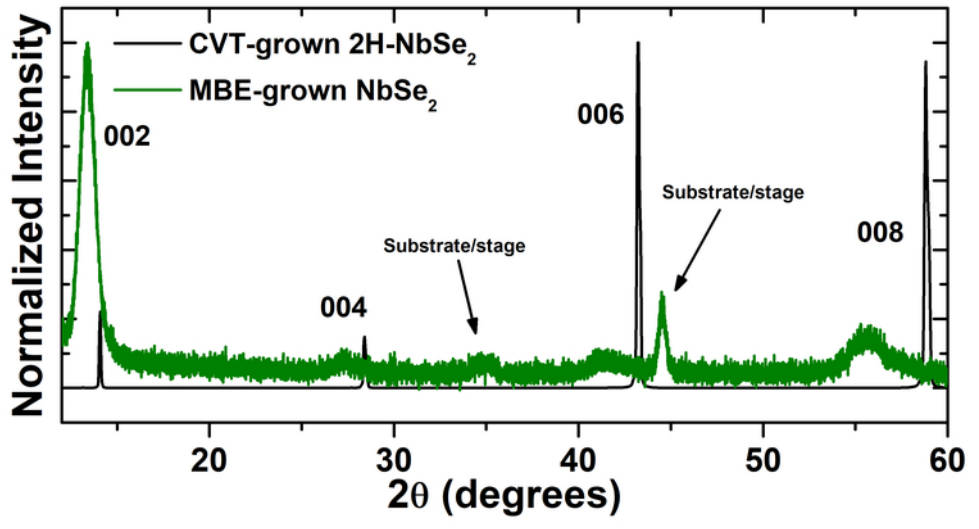
17. M. M. Ugeda, A. J. Bradley, Y. Zhang, S. Onishi, Y. Chen, W. Ruan, C. Ojeda-Aristizabal, H. Ryu, M. T. Edmonds, H.-Z. Tsai, A. Riss, S.-K. Mo, D. Lee, A. Zettl, Z. Hussain, Z.-X. Shen and M. F. Crommie, *Nature Physics* **12** (1), 92-97 (2016).
18. J. Á. Silva-Guillén, P. Ordejón, F. Guinea and E. Canadell, *2D Materials* **3** (3), 035028 (2016).
19. M. Liu, J. Leveillee, S. Lu, J. Yu, H. Kim, C. Tian, Y. Shi, K. Lai, C. Zhang, F. Giustino and C.-K. Shih, *Science Advances* **7** (47), eabi6339.
20. C.-Z. Xu, X. Wang, P. Chen, D. Flötotto, J. A. Hlevyack, M.-K. Lin, G. Bian, S.-K. Mo and T.-C. Chiang, *Physical Review Materials* **2** (6), 064002 (2018).
21. Y. Nakata, K. Sugawara, A. Chainani, H. Oka, C. Bao, S. Zhou, P.-Y. Chuang, C.-M. Cheng, T. Kawakami, Y. Saruta, T. Fukumura, S. Zhou, T. Takahashi and T. Sato, *Nature Communications* **12** (1), 5873 (2021).
22. X. Xie, D. Lin, L. Zhu, Q. Li, J. Zong, W. Chen, Q. Meng, Q. Tian, S.-C. Li, X. Xi, C. Wang and Y. Zhang, *Chinese Physics Letters* **38** (10), 107101 (2021).
23. Z.-Y. Liu, S. Qiao, B. Huang, Q.-Y. Tang, Z.-H. Ling, W.-H. Zhang, H.-N. Xia, X. Liao, H. Shi, W.-H. Mao, G.-L. Zhu, J.-T. Lü and Y.-S. Fu, *Nano Letters* **21** (16), 7005-7011 (2021).
24. H. Yang, T. Zhang, Z. Huang, Y. Chen, X. Song, X. Hao, H. Yang, X. Wu, Y. Zhang, L. Liu, H.-J. Gao and Y. Wang, *ACS Nano* **16** (1), 1332-1338 (2022).
25. M. Sidoumou, S. Merazka, A. Gómez-Herrero, M. Kars and R. Thierry, *PeerJ Inorganic Chemistry* **3** (2), 1-13 (2021).
26. T. Shimada, H. Nishikawa, A. Koma, Y. Furukawa, E. Arakawa, K. Takeshita and T.-i. Matsushita, *Surface Science* **369** (1), 379-384 (1996).
27. T. Zhu, P. M. Litwin, M. G. Rosul, D. Jessup, M. S. Akhanda, F. F. Tonni, S. Krylyuk, A. V. Davydov, P. Reinke, S. J. McDonnell and M. Zebarjadi, *Materials Today Physics* **27** (100789), 1-9 (2022).
28. K. M. Freedy, P. M. Litwin and S. J. McDonnell, *ECS Transactions* **77** (8), 11-25 (2017).
29. R. Kilaas, *Journal of Microscopy* **190** (1-2), 45-51 (1998).
30. H. Topsoe, *Bulletin* **472** (13), 63 (1968).
31. B. H. Toby and R. B. Von Dreele, *Journal of Applied Crystallography* **46** (2), 544-549 (2013).
32. J. B. Nelson and D. P. Riley, *Proceedings of the Physical Society* **57** (3), 160 (1945).
33. K. Momma and F. Izumi, (*Journal of Applied Crystallography*, 2011), Vol. **44**, 1272-1276.
34. M. Bonilla, S. Kolekar, J. Li, Y. Xin, P. M. Coelho, K. Lasek, K. Zborecki, D. Lizzit, E. Tosi, P. Lacovig, S. Lizzit and M. Batzill, *Advanced Materials Interfaces* **7** (15), 2000497 (2020).
35. O. Khyzhun, *Metallofizika i Noveishie Tekhnologii* **24**, 141-149 (2002).
36. M. H. van Maaren and H. B. Harland, *Physics Letters A* **29** (9), 571-573 (1969).
37. F. Calavalle, P. Dreher, A. P. Surdendran, W. Wan, M. Timpel, R. Verucchi, C. Rogero, T. Bauch, F. Lombardi, F. Casanova, M. V. Nardi, M. M. Ugeda, L. E. Hueso and M. Gobbi, *Nano Letters* **21** (1), 136-143 (2021).
38. C. Chen, P. Das, E. Aytan, W. Zhou, J. Horowitz, B. Satpati, A. A. Balandin, R. K. Lake and P. Wei, *ACS Applied Materials & Interfaces* **12** (34), 38744-38750 (2020).
39. F. Kadijk and F. Jelinek, *Journal of the Less Common Metals* **23** (4), 437-441 (1971).

This is the author's peer reviewed, accepted manuscript. However, the online version of record will be different from this version once it has been copyedited and typeset.

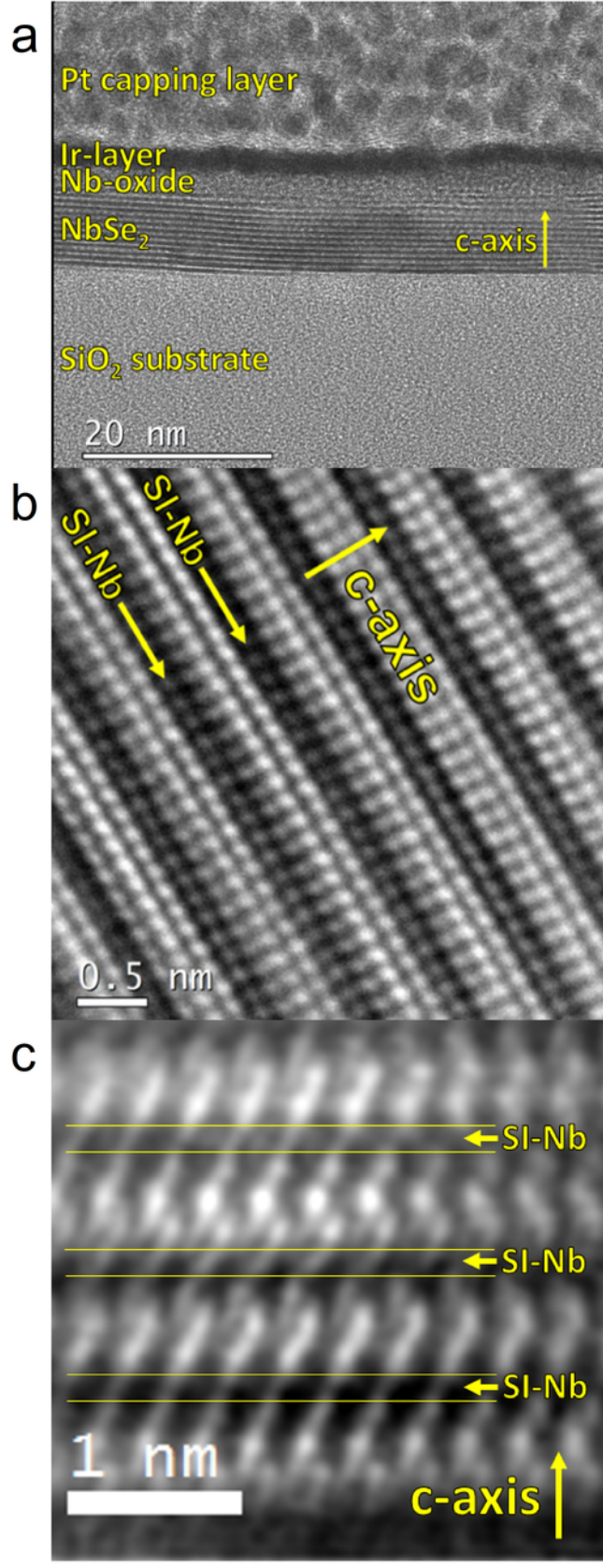
PLEASE CITE THIS ARTICLE AS DOI: 10.1116/6.0002593



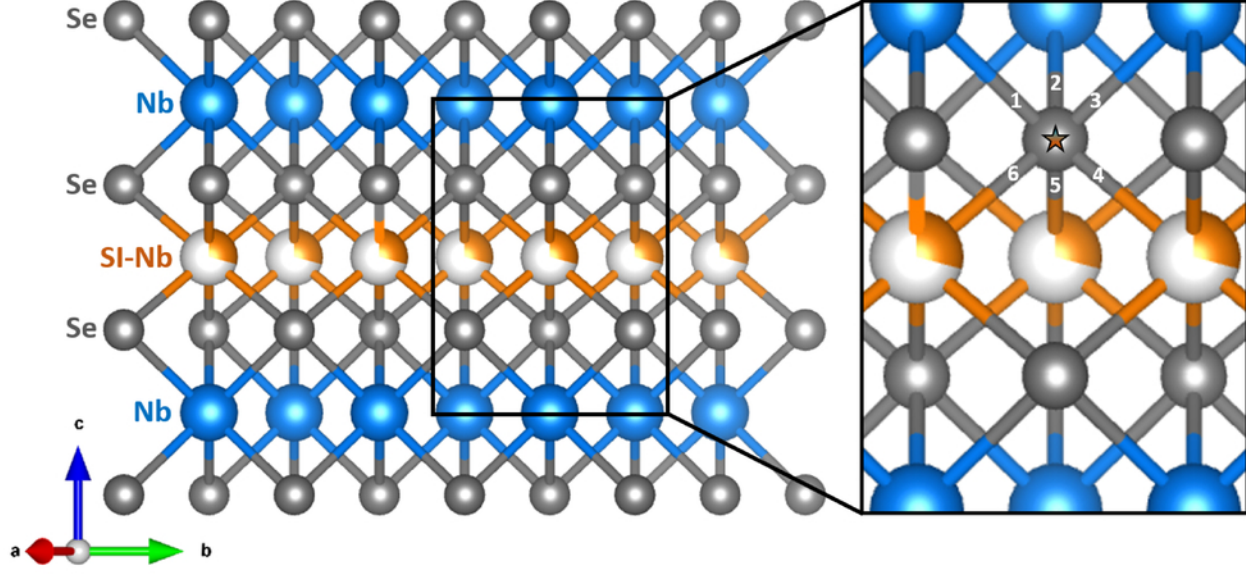
This is the author's peer reviewed, accepted manuscript. However, the online version of record will be different from this version once it has been copyedited and typeset.  
PLEASE CITE THIS ARTICLE AS DOI: 10.1116/6.0002593



This is the author's peer reviewed, accepted manuscript. However, the online version of record will be different from this version once it has been copyedited and typeset.  
PLEASE CITE THIS ARTICLE AS DOI: 10.1116/6.0002593

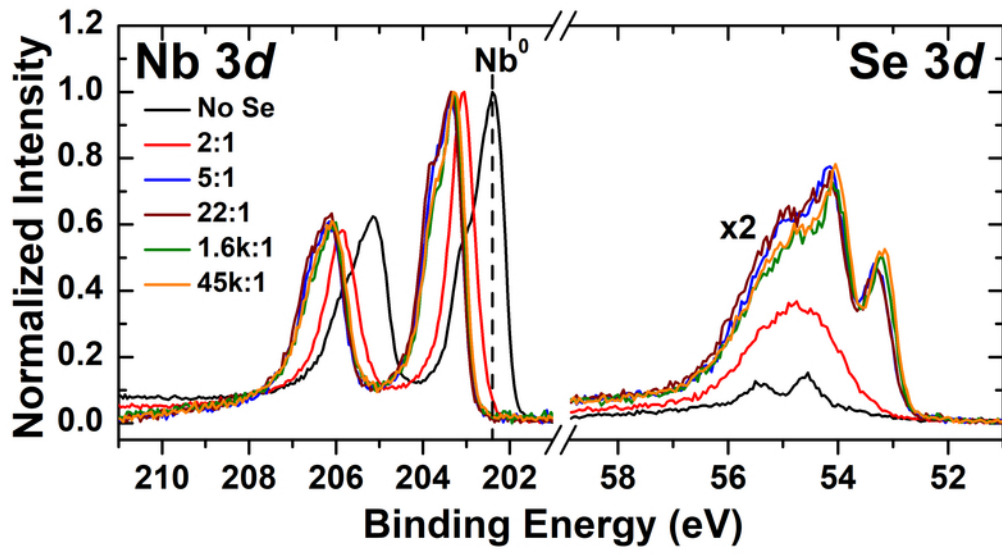


This is the author's peer reviewed, accepted manuscript. However, the online version of record will be different from this version once it has been copyedited and typeset.  
PLEASE CITE THIS ARTICLE AS DOI: 10.1116/6.0002593



This is the author's peer reviewed, accepted manuscript. However, the online version of record will be different from this version once it has been copyedited and typeset.

PLEASE CITE THIS ARTICLE AS DOI: 10.1116/6.0002593



This is the author's peer reviewed, accepted manuscript. However, the online version of record will be different from this version once it has been copyedited and typeset.  
PLEASE CITE THIS ARTICLE AS DOI: 10.1116/6.0002593

